

# Advanced 3D Monte Carlo Algorithms for Biophotonic and Medical Applications

Lewis McMillan



University of  
St Andrews

This thesis is submitted in partial fulfilment for the degree of  
PhD  
at the  
University of St Andrews

March 2019



# Declaration

I, Lewis McMillan, hereby certify that this thesis, which is approximately \*\*\*\*\* words in length, has been written by me, that it is the record of work carried out by me, or principally by myself in collaboration with others as acknowledged, and that it has not been submitted in any previous application for a higher degree.

I was admitted as a research student in September 2015 and as a candidate for the degree of PhD in September 2015; the higher study for which this is a record was carried out in the University of St Andrews between 2015 and 2019.

Date ..... Signature of candidate .....

I hereby certify that the candidate has fulfilled the conditions of the Resolution and Regulations appropriate for the degree of PhD in the University of St Andrews and that the candidate is qualified to submit this thesis in application for that degree.

Date ..... Signature of supervisor .....

Date ..... Signature of supervisor .....



# Abstract

Lorem ipsum dolor sit amet, consectetur adipiscing elit. Ut purus elit, vestibulum ut, placerat ac, adipiscing vitae, felis. Curabitur dictum gravida mauris. Nam arcu libero, nonummy eget, consectetur id, vulputate a, magna. Donec vehicula augue eu neque. Pellentesque habitant morbi tristique senectus et netus et malesuada fames ac turpis egestas. Mauris ut leo. Cras viverra metus rhoncus sem. Nulla et lectus vestibulum urna fringilla ultrices. Phasellus eu tellus sit amet tortor gravida placerat. Integer sapien est, iaculis in, pretium quis, viverra ac, nunc. Praesent eget sem vel leo ultrices bibendum. Aenean faucibus. Morbi dolor nulla, malesuada eu, pulvinar at, mollis ac, nulla. Curabitur auctor semper nulla. Donec varius orci eget risus. Duis nibh mi, congue eu, accumsan eleifend, sagittis quis, diam. Duis eget orci sit amet orci dignissim rutrum.

Nam dui ligula, fringilla a, euismod sodales, sollicitudin vel, wisi. Morbi auctor lorem non justo. Nam lacus libero, pretium at, lobortis vitae, ultricies et, tellus. Donec aliquet, tortor sed accumsan bibendum, erat ligula aliquet magna, vitae ornare odio metus a mi. Morbi ac orci et nisl hendrerit mollis. Suspendisse ut massa. Cras nec ante. Pellentesque a nulla. Cum sociis natoque penatibus et magnis dis parturient montes, nascetur ridiculus mus. Aliquam tincidunt urna. Nulla ullamcorper vestibulum turpis. Pellentesque cursus luctus mauris.



# Acknowledgements

Lorem ipsum dolor sit amet, consectetur adipiscing elit. Ut purus elit, vestibulum ut, placerat ac, adipiscing vitae, felis. Curabitur dictum gravida mauris. Nam arcu libero, nonummy eget, consectetur id, vulputate a, magna. Donec vehicula augue eu neque. Pellentesque habitant morbi tristique senectus et netus et malesuada fames ac turpis egestas. Mauris ut leo. Cras viverra metus rhoncus sem. Nulla et lectus vestibulum urna fringilla ultrices. Phasellus eu tellus sit amet tortor gravida placerat. Integer sapien est, iaculis in, pretium quis, viverra ac, nunc. Praesent eget sem vel leo ultrices bibendum. Aenean faucibus. Morbi dolor nulla, malesuada eu, pulvinar at, mollis ac, nulla. Curabitur auctor semper nulla. Donec varius orci eget risus. Duis nibh mi, congue eu, accumsan eleifend, sagittis quis, diam. Duis eget orci sit amet orci dignissim rutrum.

Nam dui ligula, fringilla a, euismod sodales, sollicitudin vel, wisi. Morbi auctor lorem non justo. Nam lacus libero, pretium at, lobortis vitae, ultricies et, tellus. Donec aliquet, tortor sed accumsan bibendum, erat ligula aliquet magna, vitae ornare odio metus a mi. Morbi ac orci et nisl hendrerit mollis. Suspendisse ut massa. Cras nec ante. Pellentesque a nulla. Cum sociis natoque penatibus et magnis dis parturient montes, nascetur ridiculus mus. Aliquam tincidunt urna. Nulla ullamcorper vestibulum turpis. Pellentesque cursus luctus mauris.

# Contents

<b>Declaration</b>	<b>iii</b>
<b>Abstract</b>	<b>v</b>
<b>Acknowledgements</b>	<b>vii</b>
<b>Abbreviations</b>	<b>ix</b>
<b>List of Figures</b>	<b>xi</b>
<b>1 Computational Modelling of Tissue Ablation</b>	<b>1</b>
1.1 Introduction and Background . . . . .	1
1.2 Methods . . . . .	2
1.2.1 Monte Carlo radiation transport (MCRT) . . . . .	2
1.2.2 Heat Transport . . . . .	3
1.2.3 Tissue Damage . . . . .	10
1.2.4 Validation . . . . .	13
1.3 <i>In silico</i> results . . . . .	15
1.3.1 Introduction . . . . .	15
1.3.2 Results . . . . .	16
1.3.2.1 Investigating Initial Temperature . . . . .	23
1.3.2.2 Investigating Voxel Temperature After Ablation . . . . .	24
1.4 Application of Model for Spy Disposal . . . . .	26
1.5 Conclusion . . . . .	26



# Abbreviations

$T_a$  ablation temperature.

**AMR** adaptive mesh refinement.

**FDM** finite difference method.

**MCRT** Monte Carlo radiation transfer.

**OCT** optical coherence tomography.

**PDT** photo-dynamic therapy.

# List of Figures

- 1.1 Flowchart of the tissue ablation algorithm.
- 1.2 Red lines are packet paths within a voxel. Black lines packet paths out with the voxel. Red packet paths, weighted by  $\mu_a$ , are summed up to calculate the absorbed energy within each voxel.
- 1.3 Finite difference method stencil for simple explicit scheme.
- 1.4 Computational domain decomposition. Total computational domain (red outline) is evenly divided between cores in the CPU. This is done via layers of the domain in the z direction. Information is passed to/from cores via the “halo swap” process (see Fig. 1.5).
- 1.5 Halo swapping. Process A updates the area in red and blue on the left. It updates the blue area which is sent to process B as B’s “halo”. Process B cannot update its own halo, but rather updates the halo for process A.
- 1.6 Figure shows the speed up gained by parallelisation of the heat simulation using the “halo swapping” technique, for various sizes of computational domain (voxels). Data taken from a Intel Xeon E3-1245 v5, 8 cores @ 3.5GHz machine.
- 1.7 Ablation of a dog aorta, as viewed under a microscope. Steam vacuoles are clearly visible either side of the ablation area. Carbonisation is also evident at the edges of the ablation fronts. Adapted from [15].
- 1.8 Temperature of the cube for various times, comparing between analytical solution and numerical method.
- 1.9 Simulation of 81 pixel beams. Figure a) shows a a slice through the optical properties at the end of the simulation in the z-y plane. Figure b) shows the optical properties in the x-y plane at the top surface. Yellow is unchanged tissue, and purple is completely ablated tissue. Figure shows that the ablation craters do not overlap one another.
- 1.10 Simulation of 70 W CO<sub>2</sub> ablative laser, with a circular beam profile. Crater depths as a function of pixel beam energy for various ablation temperature ( $T_a$ )’s.
- 1.11 Simulation of 70 W CO<sub>2</sub> ablative laser, with a Gaussian beam profile. Crater depths as a function of pixel beam energy for various  $T_a$ ’s.
- 1.12 Temperature bore hole through centre of medium as a function of time, for  $T_a=500^\circ C$ .
- 1.13 Tissue thermal damage around the ablation crater (white). Thermal tissue damage values of 3 refer to 3<sup>rd</sup> degree burns, 2 to 2<sup>nd</sup>, and 1 to 1<sup>st</sup> degree burns respectively. P is the power in Watts,  $T_a$  is the ablation temperature in Kelvin, and  $E_p$  is the energy per pixel beam in mJ.
- 1.14 Figure shows the maximum horizontal extent of thermal damage as a function of energy per pixel beam, for different  $T_a$ ’s.
- 1.15 Figure show the time taken for 1<sup>st</sup>, 2<sup>nd</sup>, and 3<sup>rd</sup> to occur as a function of depth, for a range of  $T_a$ ’s at 400 mJ.

- 1.16 Figure show the time taken for 1<sup>st</sup>, 2<sup>nd</sup>, and 3<sup>rd</sup> to occur as a function of depth, for a range of  $T_a$ 's at 50 mJ.
- 1.17 Comparison of the different pulse profiles trialled for a pulselength of 0.2 s.
- 1.18 Comparison of various pulse shapes for the pixel beams.
- 1.19 Comparison of ablation depths for different initial temperatures in the porcine skin.
- 1.20 Comparison of maximum horizontal damage distance for different initial porcine skin temperatures.
- 1.21 Comparison of different voxel temperatures after ablation. Half refers to setting the temperature of a voxel to half that of the ablation temperature. Room refers to room temperature, and ablation leaves the temperature at the ablation temperature.
- 1.22 Still image of the iconic laser scene in the film Goldfinger. Copyrights Eon Productions.



# Chapter 1

# Computational Modelling of Tissue Ablation

## 1.1 Introduction and Background

This chapter uses Monte Carlo radiation transfer (MCRT) techniques coupled to a heat transfer simulation, to study the thermal damage to tissue due to a laser, with its power spread over many beams to leave viable tissue around zones of damaged/necrotic tissue [1]. This class of laser is called a fractionated ablative laser. This chapter presents experimental work carried out on porcine tissue by our collaborators at the University of Dundee and the photobiology department at Ninewells Hospital, along side my computational model of tissue ablation.

Ablative lasers are used in a wide variety of medical procedures including: coagulating scalpels, port wine stain removal, tattoo removal, hair removal, and skin rejuvenation [2–6]. One class of laser used in these procedures are ablative lasers. Ablative lasers are usually high powered lasers ( $>30$  W) targeted at a specific chromophore in the skin, to partially or fully remove layers of skin. These types of lasers are commonly used for aesthetic procedures such as: skin rejuvenation [6], and removal of various diseases such as Rhinophyma [7] or lesions/nodules [8]. Ablative lasers have also been recently investigated as a means of better drug penetration into the skin for various therapies such as photo-dynamic therapy (PDT). The ablative laser “drills” holes in the skin, which allows topical treatments to better diffuse into the skin [9].

One downside to using lasers to remove tissue, is that unlike a scalpel where the surgeon has full control of the depth of the incision, ablative lasers are not as predictable. Lasers can cause thermal damage to the surrounding areas, leading to potentially unwanted effects, though some applications of ablative lasers utilise the thermal damage, particularly aesthetic procedures [10].

Currently, the only reliable method to measure the depth of the ablative holes, is via a biopsy, which is an invasive procedure. In this work an optical coherence tomography (OCT) system is used to measure the ablative crater non-invasively *in-vivo*. The OCT measurements are then compared to a computational model developed as part of this project. It is hoped this computational model could be used to predict the depth of the ablative crater when using a certain laser power for various different applications such as: laser assisted drug delivery, and various cosmetic applications.

## 1.2 Methods

To replicate the experimental work *in silico*, the numerical model has three main portions. The first is the MCRT code that models light transport through tissue so that we can calculate the laser energy deposited as a function of time and space. The second, a finite difference method (FDM) which is used to calculate the heat diffusion within the tissue due to the absorbed laser energy. Finally, a tissue damage model to track the tissue damage caused by the laser. All these individual functions are connected together to create a full numerical model.

### 1.2.1 Monte Carlo radiation transport (MCRT)

MCRT is used here to calculate the energy deposited by the laser. This is then passed to the heat transport simulation, which calculates the heat diffusion in the medium. The algorithm for the three coupled simulations is presented in Fig. 1.1.

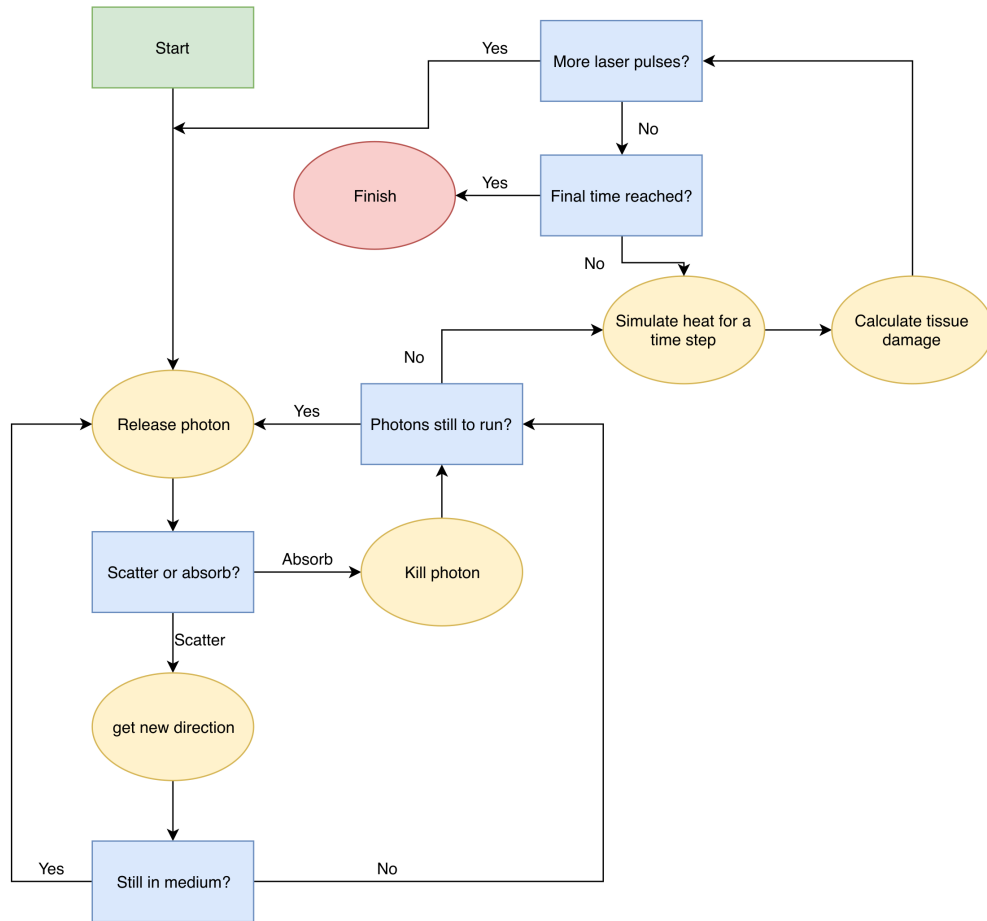


**Figure 1.1:** Flowchart of the tissue ablation algorithm.

The MCRT algorithm is largely the same as described in ??, with some important adjustments.

The first adjustment is that the path length counter for fluence is changed to track absorbed energy. This is achieved by multiplying the pathlength in a voxel by the absorption coefficient of that voxel. Figure 1.2 show this process graphically, and Equation (1.34) shows the mathematical expression:

$$E_i^{abs} = \frac{P}{NV_i} \sum \mu_{a,i} s \quad (1.1)$$

Where:

$E_i^{abs}$  is the energy absorbed in the  $i^{th}$  voxel [ $Js^{-1}m^{-3}$ ];

P is power [W];

N is the number of packets, representing a power, P;

$V_i$  is the volume of the  $i^{th}$  voxel [ $m^{-3}$ ];

$\mu_{a,i}$  is the absorption coefficient of the  $i^{th}$  voxel [ $cm^{-1}$ ];

and s is the pathlength of a packet through the  $i^{th}$  voxel [cm].

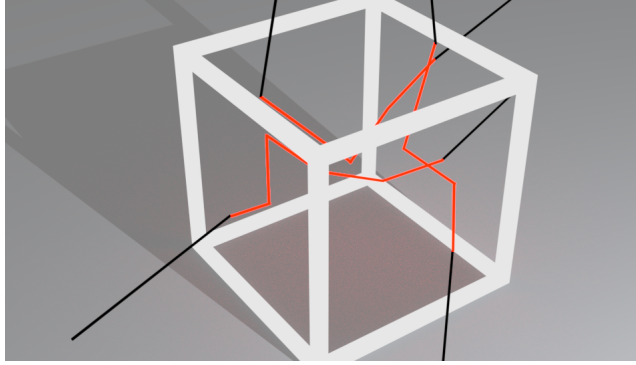


**Figure 1.2:** Red lines are packet paths within a voxel. Black lines packet paths out with the voxel. Red packet paths, weighted by  $\mu_a$ , are summed up to calculate the absorbed energy within each voxel.

This grid of absorbed energy is then passed to the heat transport portion of the simulation, so that the heat diffusion in the porcine tissue can be calculated.

The next adjustment to the MCRT algorithm is that the MCRT algorithm is run for every heat simulation time step, as the medium could change at every time step due to the optical, and thermal properties changing as a function of tissue damage.

Finally, to match the experiment undertaken the medium and laser for the *in-silico* experiments must match the practical experiments. As the laser used in the experiments emits an infra-red wavelength ( $10.6 \mu m$ ), the optical properties are dominated by the water content of the tissue. Due to this it is assumed that there is just absorption in the medium, with no scattering. Further discussion can be found in Section 1.3.1. The laser in some of the *in silico* modelling, has multiple beams and the source photon packet routine is adjusted to accommodate this when needed.

## 1.2.2 Heat Transport

The diffusion of heat can be modelled using the heat equation (Eq. (1.2)), which is derived from Fourier's law and the principle of conservation of energy [11]. The standard heat equation is a partial differential equation of the parabolic form. Solutions and analytical methods are readily

available for lower dimensions (i.e. 1D heat diffusion), but for higher dimensions, numerical models must be used for all except the simplest problems. The simplest form of the heat equation is shown below:

$$\rho c_p \frac{\partial T}{\partial t} = \nabla \cdot (\kappa \nabla T) + \dot{q} \quad (1.2)$$

Where:

- $T(x, y, z, t)$  is the temperature as a function of time and space  $[K]$ ;
- $\kappa$  is the thermal conductivity  $[Wm^{-1}K^{-1}]$ ;
- $\rho$  is the density  $[Kgm^{-3}]$ ;
- $c_p$  the specific heat capacity  $[JK^{-1}]$ ;
- $\dot{q}(x, y, z, t)$  is the source/sink term as a function of time and space  $[Wm^{-3}]$ .

Equation (1.2) is for a homogeneous system where the thermal properties do not change as a function of time, space and temperature. However, to model a moving ablation front the nonlinear heat equation must be used, where the thermal properties can be a function of time, space and temperature (Eq. (1.3)).

$$\frac{\partial T}{\partial t} = \frac{1}{(\rho c_p)_\xi} (\nabla k_\xi T + k_\xi \nabla^2 T) + \dot{q}, \quad \text{where } \xi = (i, j, k) \quad (1.3)$$

Included in Eq. (1.3) is a source and sink term,  $\dot{q}$ , to allow the modelling of heat loss/gain from external sources/sinks. The heat source in this simulation is due to the laser, and it is assumed that the only loss of heat to the surrounding medium is via conduction.

The medium is considered to be at a constant temperature of 5°C, as the porcine skin was kept cooled prior to experimental work and the simulation volume is smaller than the porcine tissue samples.

Where:

- $h$  is the heat transfer coefficient  $[Wm^{-2}K]$ ;
- $A$  is the area of the grid element, that is radiating/convecting heat away  $[m^2]$ ;
- and  $T$ , and  $T_\infty$  are the temperature in a voxel and the surrounding medium temperature respectively  $[K]$ .

As Eq. (1.3) is generally hard to solve in arbitrary geometries with complex boundary conditions, a numerical method is employed to solve it. The numerical method employed is a FDM, derived from the Taylor series, see Eq. (1.4).

A function  $f(x)$  is discretised onto a grid with  $N$  nodes a distance  $\Delta x$  apart. Equation (1.4) is then truncated and rearranged and it is assumed that the remainder term  $R_1$  is sufficiently small enough, to yield an approximation for the first derivative of a function  $f(x)$  at a point  $x_0 + \Delta x$ , see Eq. (1.5). Equation (1.5) is the so called forward difference, due to it using a point in the “forward” direction. The “backward” and central difference terms can be calculated by using a node at  $x_0 - \Delta x$  for the backward difference Eq. (1.6b). The central difference (Eq. (1.6c)) is an average of the forward and backwards differences. Expressions can also be given for the  $2^{nd}$  derivatives for backward, forward and central (forward and backward  $2^{nd}$  order equations omitted for brevity) Eq. (1.6d).

$$f(x_0 + \Delta x) = f(x_0) + \frac{f'(x_0)}{1!} \Delta x + \frac{f''(x_0)}{2!} \Delta x^2 + \dots + \frac{f^{(n)}(x_0)}{n!} \Delta x^n + R_n(x) \quad (1.4)$$

$$f'(x_0) \approx \frac{f(x_0 + \Delta x) - f(x_0)}{\Delta x} \quad (1.5)$$



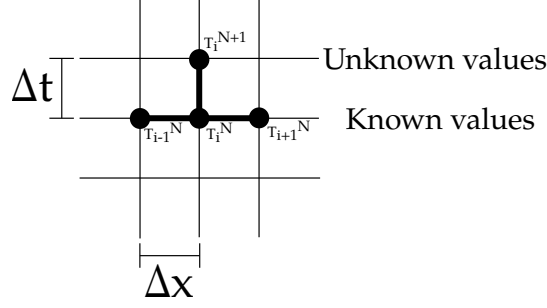


**Figure 1.3:** Finite difference method stencil for simple explicit scheme.

$$\frac{df}{dx} = \frac{f_{i+1} - f_i}{\Delta x} \quad (\text{forward}) \quad (1.6a)$$

$$\frac{df}{dx} = \frac{f_i - f_{i-1}}{\Delta x} \quad (\text{backward}) \quad (1.6b)$$

$$\frac{df}{dx} = \frac{f_{i+1} - f_{i-1}}{2\Delta x} \quad (\text{central}) \quad (1.6c)$$

$$\frac{d^2 f}{dx^2} = \frac{f_{i-1} - 2f_i + f_{i+1}}{\Delta x^2} \quad (\text{central}) \quad (1.6d)$$

Thus, the linear heat equation Eq. (1.2), in 1D, taking a 1<sup>st</sup> order forward time derivative, and a 2<sup>nd</sup> order central spatial derivative gives:

$$\frac{T_i^{n+1} - T_i^n}{\Delta t} = \alpha \frac{T_{i-1}^n - T_i^n + T_{i+1}^n}{\Delta x^2} + \frac{\dot{q}}{\rho c_p} \quad (1.7a)$$

$$T_i^{n+1} = \alpha \Delta t \frac{T_{i-1}^n - 2T_i^n + T_{i+1}^n}{\Delta x^2} + \frac{\Delta t \dot{q}}{\rho c_p} \quad (1.7b)$$

Where  $\alpha = \frac{\kappa}{\rho c}$ .

Equation (1.7b) is called the “simple explicit form of finite-difference approximation” [12]. Figure 1.3 shows the “stencil” of this scheme, where there are three known points at time  $N$ , and just one unknown at time  $N+1$ . There are various other schemes that can be used to calculate the temperature at the next time step. However, a simple explicit scheme is used here, due to its ease of implementation despite there being a constraint on the stability in comparison to an implicit method. This method is also easily scaled up to 3D with little difficulty.

For the more complicated nonlinear heat equation there is a possibility that the medium is not continuously smooth between nodes, in terms of optical and thermal properties. The two easiest methods [12] of achieving this are: (1), lag the value behind by one step, i.e  $c_p^{n+1} = c_p^n$ . (2), average  $\kappa$ ,  $\rho$ , and  $c_p$  using a half difference scheme where the thermal property used in the calculation is the thermal property half way between two nodes, i.e the average of the two nodes:

---

\*For brevity  $f(x_0 + \Delta x)$  is defined as  $f_{i+1}$ , and  $f(x_0 - \Delta x)$  as  $f_{i-1}$ , etc.

$$\kappa^\pm = \frac{\kappa_i + \kappa_{i\pm 1}}{2} \quad (1.8)$$

$$\rho^\pm = \frac{\rho_i + \rho_{i\pm 1}}{2} \quad (1.9)$$

$$c_p^\pm = \frac{c_{p,i} + c_{p,i\pm 1}}{2} \quad (1.10)$$

Thus, for the simple 1D case as in Eq. (1.7b), the thermal properties are averaged between nodes when computing the coefficients of the temperature nodes, and lag the thermal properties when adding the heat from the laser:

$$T^{N+1} = \Delta t(AT_{i-1}^N - 2BT_i^N + DT_{i+1}^N) + T_i^N + \frac{\Delta t}{\rho c_p} q_L \quad (1.11)$$

Where (in the  $x$  direction):

$$\begin{aligned} A &= \frac{\kappa^-}{\rho^- c_p^- 2\Delta x^2} \\ B &= \frac{\kappa^+}{\rho^+ c_p^+ 2\Delta x^2} \\ D &= \frac{(A + B)}{2} \end{aligned} \quad (1.12)$$

Equation (1.11) is straightforward to generalise to higher dimensions. The 3D case gives:

$$U_{xx} = (AT_{i-1,j,k}^N - 2BT_{i,j,k}^N + DT_{i+1,j,k}^N) \quad (1.13)$$

$$U_{yy} = (AT_{i,j-1,k}^N - 2BT_{i,j,k}^N + DT_{i,j+1,k}^N) \quad (1.14)$$

$$U_{zz} = (AT_{i,j,k-1}^N - 2BT_{i,j,k}^N + DT_{i,j,k+1}^N) \quad (1.15)$$

$$T_{i,j,k}^{N+1} = \Delta t (U_{xx} + U_{yy} + U_{zz}) + T_{i,j,k}^N + \frac{\Delta t}{\rho c_p} q_L \quad (1.16)$$

Where:

$T_{i,j,k}^{N+1}$  is the new temperature at node  $i, j, k$  [K];

$T_{i,j,k}^N$  is the temperature at node  $i, j, k$  at the current time step [K];

$\alpha$  is the thermal diffusivity [ $m^2 s^{-1}$ ];

$\kappa$  is the thermal conductivity [ $W/mK$ ];

$\Delta x$  etc. is the size of the grid element in the  $p^{th}$  direction [ $m$ ];

and  $A, B, D$  are the coefficients in their respective dimension (Eq. (1.12)).

Equation (1.16) gives the full numerical solution to the nonlinear heat equation with a laser heat source. This will allow the calculation of the heat diffusion in the porcine tissue due to laser heating.

As the laser used in the experimental work operates in a pulsed mode, this is accounted for in the simulation. The laser pulse shape is a triangular pulse, with the peak power,  $P_{peak}$ , and pulse length,  $\tau$  [13]. In the heat simulation there has to be an additional variable in the term  $laserOn(t) \cdot \frac{\alpha \Delta t}{\kappa} q_L$  in Eq. (1.16). This additional variable,  $laserOn(t)$ , is a boolean value and a function of time, which is defined as:

$$laserOn = \begin{cases} 1, & \text{Laser on} \\ 0, & \text{Laser off.} \end{cases}$$

In the instance where there is a train of laser pulses, the laser is turned on and off based upon the pulse frequency.

Due to a simple explicit FDM being used, the time step is constrained to make the solution stable. For a cubic 3D FDM without prescribed flux boundary conditions, this yields the constraint:  $\Delta t \leq \frac{1}{\delta\alpha}$  where  $\delta = \frac{1}{\Delta x^2} + \frac{1}{\Delta y^2} + \frac{1}{\Delta z^2}$ . Along with this time constraint, the pulse length of the laser also has to be considered. If the time step of the heat simulation is too large it will not account for the heat deposited by the laser. Thus, the timestep has to be at least an order of magnitude smaller than the shortest laser pulse.

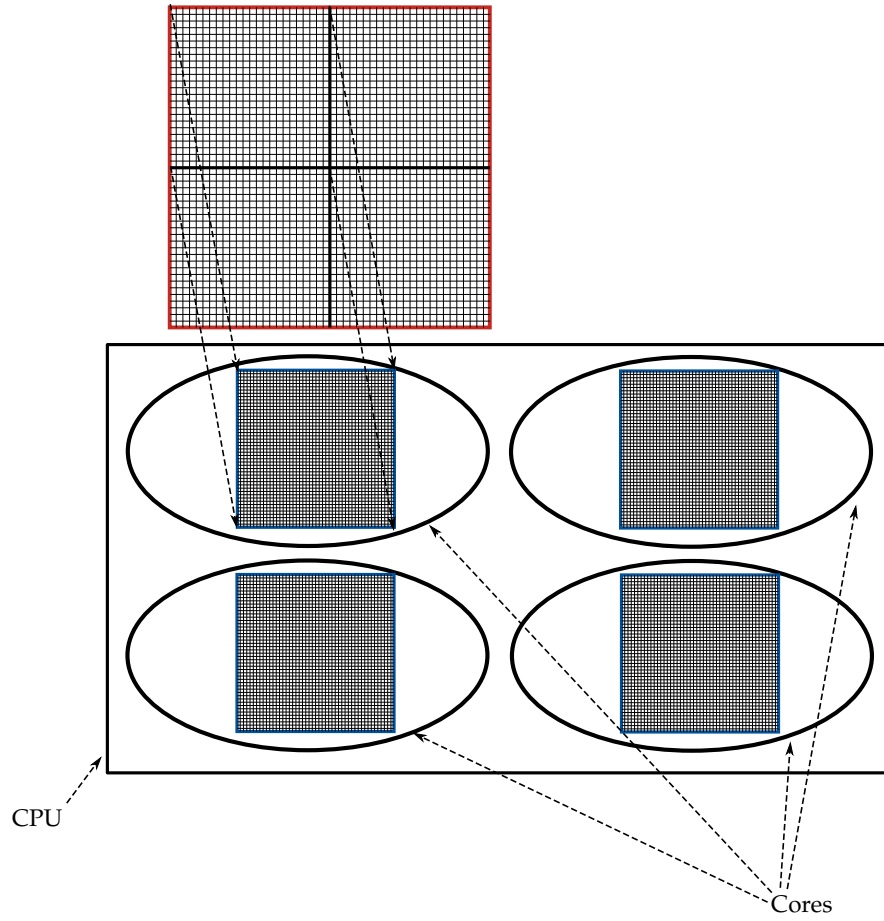
As the time step is small, and the grid resolution large, the resultant simulation is slow. Thus, the code has been fully parallelised to improve performance. Both the MCRT and heat simulation are independently parallelised.

Parallelisation of the heat simulation is more involved than the “embarrassingly parallel” class of problems where MCRT belongs. This is due to the heat simulation being dependent on neighbouring nodes to update the temperature at the current node. Thus, if the medium were to be split up on to separate cores, there would have to be communication between the cores, in order for the simulation to be completed successfully. Therefore it is not possible to take the “easy” route of running the simulation concurrently  $N$  times and collating the result at the end of all the simulations.

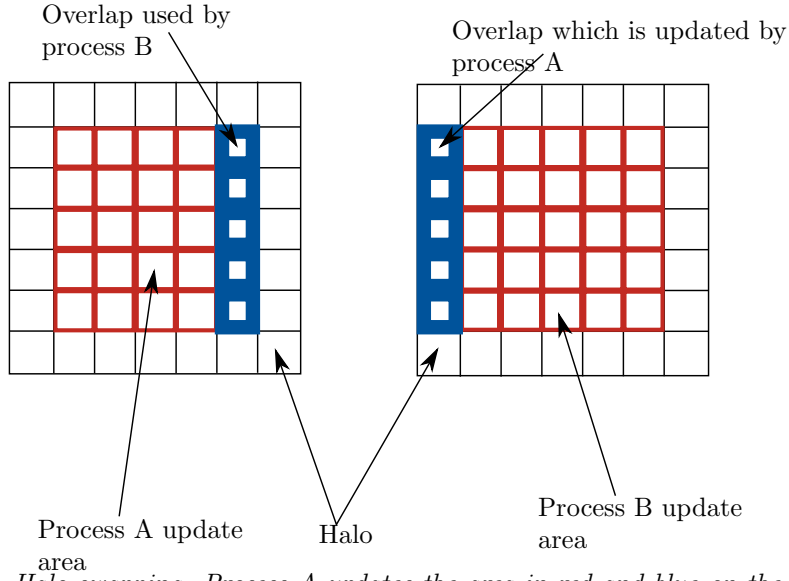
The heat simulation is parallelised using a technique called “halo swapping”. This involves splitting up the computational domain (see Fig. 1.4), in this case the tissue medium, and doing the calculations on each domain on a separate core. The “halo swapping” comes in when cores need to communicate with each other about updating their boundary temperature nodes (see Fig. 1.5).

Figure 1.6 shows the speed up gained from using the technique. The “halo swapping” technique is efficient for situations where the computational domain can be split up with large “chunks” being calculated on each core. However, if the computational domain is small, and the number of cores large then bottlenecks occur due to too much communication between cores taking place. Thus, to efficiently use “halo swapping” careful thought has to be given to the size of the computational domain, and the number of cores running the simulation. Evidence of this bottlenecking can be seen in Fig. 1.6 for problems where the size of the grid, in voxels, is  $40^3$  and  $24^3$ . These problems also show superlinear speed up, for certain number of cores. This is not unfeasible, due to several reasons, in particular the underlying computer architecture [14].

After one time step of the heat simulation has been completed, the temperature grid is passed to the tissue damage portion of the simulation to calculate the tissue damage that may have accrued during the heat simulation time step.



**Figure 1.4:** Computational domain decomposition. Total computational domain (red outline) is evenly divided between cores in the CPU. This is done via layers of the domain in the  $z$  direction. Information is passed to/from cores via the “halo swap” process (see Fig. 1.5).



**Figure 1.5:** Halo swapping. Process A updates the area in red and blue on the left. It updates the blue area which is sent to process B as B's "halo". Process B cannot update its own halo, but rather updates the halo for process A.

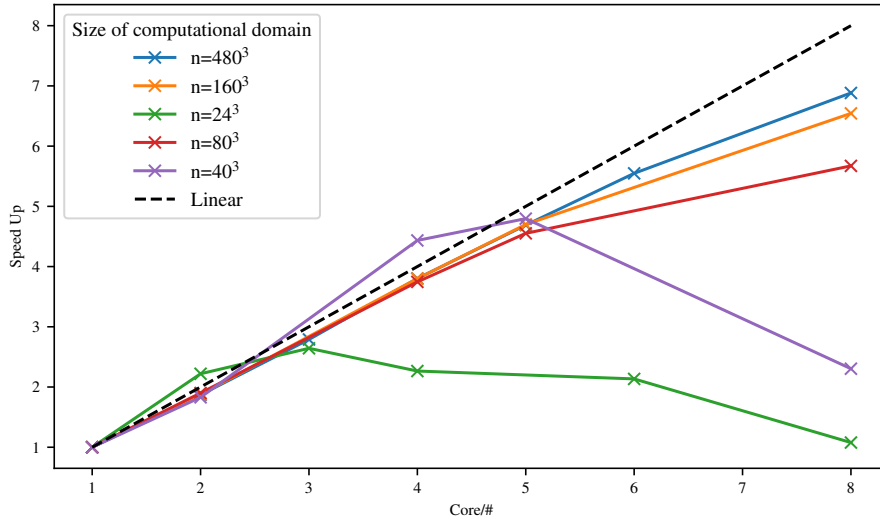


**Figure 1.6:** Figure shows the speed up gained by parallelisation of the heat simulation using the "halo swapping" technique, for various sizes of computational domain (voxels). Data taken from a Intel Xeon E3-1245 v5, 8 cores @ 3.5GHz machine.

### 1.2.3 Tissue Damage

#### Introduction

The final portion of the simulation is the tissue damage model. To be able to model damage to the tissue, the process tissue undergoes upon heating due to the laser needs to be able to be described.

When the laser is turned on, the temperature starts to rise within the tissue due to the absorption of photons by the tissue. The temperature rise causes damage to the tissue when above a threshold temperature,  $T_d$ , approximately  $43^\circ\text{C}$  [15]. From the temperature,  $T_d$ , four main areas of tissue damage are defined:

$$T = \begin{cases} \text{coagulation,} & T_d \leq T \leq 100^\circ\text{C} \\ \text{water boils,} & T = 100^\circ\text{C} \\ \text{carbonisation,} & 100^\circ\text{C} \leq T \leq T_a \\ \text{ablation,} & T = T_a. \end{cases} \quad (1.17)$$

The area of tissue damage termed ‘‘coagulation’’ is a multifaceted process. At  $43^\circ\text{C}$  -  $50^\circ\text{C}$ , bonds break within cell membranes, causing ruptures and some cell death [15, 16]. This process is usually termed *hyperthermia*. Around  $50^\circ\text{C}$ , enzyme activity decreases, cells become immobile, and various cell repair mechanisms are disabled, leading to increased cell death. When temperatures exceed  $60^\circ\text{C}$ , proteins become denatured. Thermal denaturation is a structural and functional change in a protein due to the heating it undergoes. This means they change from a highly organised structure with specific purposes, to disorganised structures with little to no function at all [17].

The next stage in the tissue damage process is the vaporisation of water. As the temperature of the tissue starts to approach  $100^\circ\text{C}$  (at 1 atm), water starts to vaporise. If the vaporised water cannot escape the tissue it forms steam vacuoles, small pockets of steam. These vacuoles can easily be seen when viewing tissue samples after tissue has been treated with a high powered laser (see Fig. 1.7). In certain conditions these steam pockets can explode [18].

The third stage of tissue damage is carbonisation of the tissue. This occurs when most of the water has boiled off, leaving the remaining tissue to heat up and reduce to its elemental carbon form. This carbonisation of tissue, when it occurs, is generally only a thin layer of  $5\text{-}20\ \mu\text{m}$  [15, 19].

The final stage of tissue damage is the removal of the remaining tissue, i.e tissue ablation. There is no agreement in the literature how tissue undergoes ablation with several methods proposed. The three main methods are: photochemical, thermal, and explosive [20–22]. Photochemical ablation is when the energy of a photon from the irradiating laser, is sufficient enough that it excites the electronic state of the tissues molecules into an anti-bonding state, leading to broken bonds and conversion from electronic energy into kinetic energy, and thus ablation. Thermal ablation is where tissue is heated sufficiently so that tissue vaporisation takes place. Finally, explosive ablation is an extreme version of thermal ablation. Explosive ablation occurs when large amounts of energy is deposited in a small time scale, so that none of the energy can thermally diffuse away, resulting in explosive ablation. Photochemical ablation, is usually applied to UV laser ablation, whereas thermal and explosive ablation regimes are the more likely candidates for IR ablation which is considered here.

The theoretical models behind explosive and thermal ablation models are also not well understood, with many models proposed to try to and explain experimental results. These models range from heuristic models to sophisticated models that relate the underlying physical mechanisms to ablation damage. The two main heuristic models are: the blow off model, and the

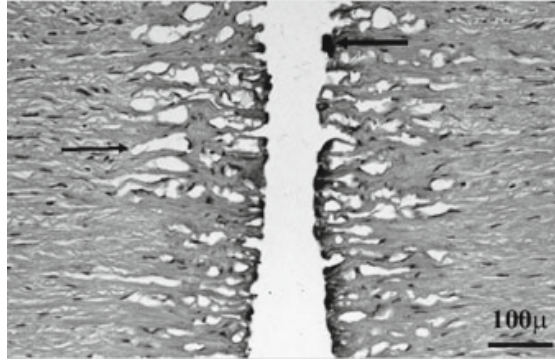


**Figure 1.7:** Ablation of a dog aorta, as viewed under a microscope. Steam vacuoles are clearly visible either side of the ablation area. Carbonisation is also evident at the edges of the ablation fronts. Adapted from [15].

steady state model. The blow off model assumes that there is thermal confinement (i.e. no propagation of heat in time  $t$ ), and that material is removed after the laser irradiation. There is a radiant threshold that has to be met to ablate material, and that Beer-Lambert's law describes the spatial distribution of light. For laser pulses of  $< 10$  ns, these conditions are normally met. However, for lasers with pulse length larger than this, these conditions are not usually met [23–25].

The steady state heuristic model, assumes that the pulse length is of the order of  $ms$  or larger, that material starts to be removed shortly after laser irradiation begins, and that some radiant threshold exists in order for ablation to begin. The steady state model also assumes that a fixed energy is required to remove a unit of tissue [23]. However, this does not always hold, as there are many circumstances where there is no one fixed energy, but rather many energies (due to various phase changes) that must be met in order for ablation to occur. There are also many other sophisticated models, that try to describe what happens physically when ablation occurs [26–28].

Due to the above mentioned reasons, there is no defined ablation temperature. The literature however, does suggest that it takes place when the tissue temperature is between  $177\text{ }^{\circ}\text{C}$  and  $500\text{ }^{\circ}\text{C}$  [27, 29, 30].

To model all these tissue damage processes the tissue damage model is split into two sections: coagulation damage and “physical” damage. Coagulation damage has no effect on the tissue's bulk optical or thermal properties. “Physical” damage changes the tissue optical and thermal properties.

## Modelling coagulation damage

With the description of the various processes that tissue undergoes during ablation, a numerical model of these processes can be created. First to model the full extent of the damage done under  $100^{\circ}\text{C}$ , i.e. in the coagulation regime, the Arrhenius damage model is used. The Arrhenius damage model was originally used as a kinetic model of reaction products in chemistry [31]. It has since been adapted by various authors for modelling tissue damage, and is the *de facto* standard [32, 33]. These authors and various others, adapted this model by fitting Eq. (1.18) to experimental data for burn damage. The two parameters fitted are  $A$ , the frequency factor, and  $\Delta E$ , the activation energy.

$$\Omega(t) = \int_{t_i}^{t_f} A e^{(-\frac{\Delta E}{RT})} d\tau \quad (1.18)$$

Where:

- $\Omega$  is the damage value [-];
- $A$  is “frequency factor” [ $s^{-1}$ ];
- $\Delta E$  is activation energy [ $Jmol^{-1}$ ];
- $R$  is the universal gas constant [ $Jmol^{-1}K^{-1}$ ];
- $T$  is the temperature [ $K$ ];
- and  $t_i$  and  $t_f$  are the initial time and final time at  $t_{crit}$ .

It is reported that a value of  $\Omega$  of 0.53, 1.0, and  $10^4$  relate to first, second, and third degree burns respectively [34]. The Arrhenius damage model is used to better understand the amount of damage caused by the laser in the non-ablated areas of tissue. Values of  $A = 3.1 \times 10^{98}$  and  $\Delta E = 6.3 \times 10^5$  are adopted [30, 32, 35].

### Modelling physical tissue damage

As tissue mostly consists of water [36] when the temperature of the tissue approaches  $100^\circ C$  (at 1 atm), water in the tissue begins to boil off. This acts as a large heat sink for the absorbed laser energy, slowing down the rate of ablation. The energy required to boil the water is  $Q_{vapor} = m_v \cdot L_v$ , where  $m_v$  is the mass of a voxel, and  $L_v$  is the latent heat of vaporisation. The energy to boil off the water is provided via the laser and heat diffusing into the voxel:

$$Q_{vapor} = \underbrace{laserOn(t) \cdot \dot{q} \cdot \Delta t \cdot V_{i,j,k}}_{\text{laser heating}} + \underbrace{c \cdot M_{i,j,k} \cdot \Delta T}_{\text{heat diffusion}} \quad (1.19)$$

Where:

$Q_{vapor}$  is the current energy in Joules that has been used to boil off the water in the voxel [ $J$ ];

$laserOn$  is a boolean variable that determine if the laser is on or off [-];

$\dot{q}$  is the energy absorbed by the voxel due to the laser [ $Wm^{-3}$ ];

$\Delta t$  is the timestep [ $s$ ];

$V_{i,j,k}$  is the volume of the voxel labelled  $i, j, k$  [ $m^3$ ];

$c$  is the heat capacity of the voxel [ $JK^{-1}$ ];

$M_{i,j,k}$  is the mass of the voxel labelled  $i, j, k$  [ $kg$ ];

and  $\Delta T$  is the change in temperature the voxel would undergo, if the water was not boiling off.

As water boils off, the water content of each voxel changes. This affects the absorption coefficient, density, thermal conductivity, and heat capacity. Each of these vary with water content per voxel [37];



$$W = W_{init} - \left( W_{init} \cdot \left( \frac{Q_{current}}{Q_{vaporisation}} \right) \right) \quad (1.20)$$

$$\rho = \frac{1000}{W + 0.649 \cdot P} \quad (1.21)$$

$$c_p = 4.2 \cdot 10^3 \cdot W + 1.09 \cdot 10^3 \cdot P \quad (1.22)$$

$$\kappa = \rho \cdot (6.28 \cdot 10^{-4} \cdot W + 1.17 \cdot 10^{-4} \cdot P) \quad (1.23)$$

$$\mu_a = W \cdot \mu_{water} + \mu_{protein} \quad (1.24)$$

$$(1.25)$$

Where:

$W$  is the water content (i.e  $W = 0.7$  equates to 70% water content);

$W_{init}$  is the initial water content;

$Q_{current}$  is the total energy absorbed by the  $i^{th}$  voxel since the temperature reached 100°C [J];

$P$  is the protein content (i.e  $P = 1.0 - W$ );

$\kappa$  is the Thermal conductivity [ $Wm^{-1}K^{-1}$ ];

$c_p$  is the heat capacity [ $Jkg^{-1}K^{-1}$ ];

and  $\mu_a$  is the total absorption coefficient, and  $\mu_{water}$  and  $\mu_{protein}$  are the absorption coefficients of water and protein respectively.

$T_a$  is defined as occurring between 177 and 500 °C [27, 29, 30]. At  $T_a$  the tissue is removed and the thermal, optical, and physical properties set to that of air.

The updated damaged tissue structure is then fed back to the MCRT model and the whole process repeats until the predefined time limit is reached. This whole process of photon propagation, heat diffusion and tissue damage is outlined in Fig. 1.1.

## 1.2.4 Validation

### Heat transport validation

To thoroughly validate the numerical method employed to solve the heat equation, the numerical method is compared against an easily solvable analytical case. The heat equation is solved on a cube, side  $L$ , in a surrounding medium of 0°C. The cube is initially at temperature 20°C and the temperature is calculated at various times. Thus, the boundary conditions are:

$$T(0, y, z, t) = T(x, 0, z, t) = T(x, y, 0, t) = 0^\circ C \quad (1.26)$$

$$T(L, y, z, t) = T(x, L, z, t) = T(x, y, L, t) = 0^\circ C \quad (1.27)$$

The thermal diffusivity ( $\alpha$ ), density ( $\rho$ ), and heat capacity ( $c_p$ ) are all set to 1. This corresponds to a material which has the thermal diffusivity between copper and aluminium [38, 39]. Assuming a separable solution in Cartesian coordinates yields:

$$\begin{aligned} T(x, y, z, t) = & (A_1 \cos(\alpha x) + A_1 \sin(\alpha x)) \cdot \\ & (B_1 \cos(\beta y) + B_1 \sin(\beta y)) \cdot \\ & (C_1 \cos(\gamma z) + C_1 \sin(\gamma z)) \cdot e^{-\alpha \mu^2 t} \end{aligned} \quad (1.28)$$

$$\mu^2 = \alpha^2 + \beta^2 + \gamma^2 \quad (1.29)$$

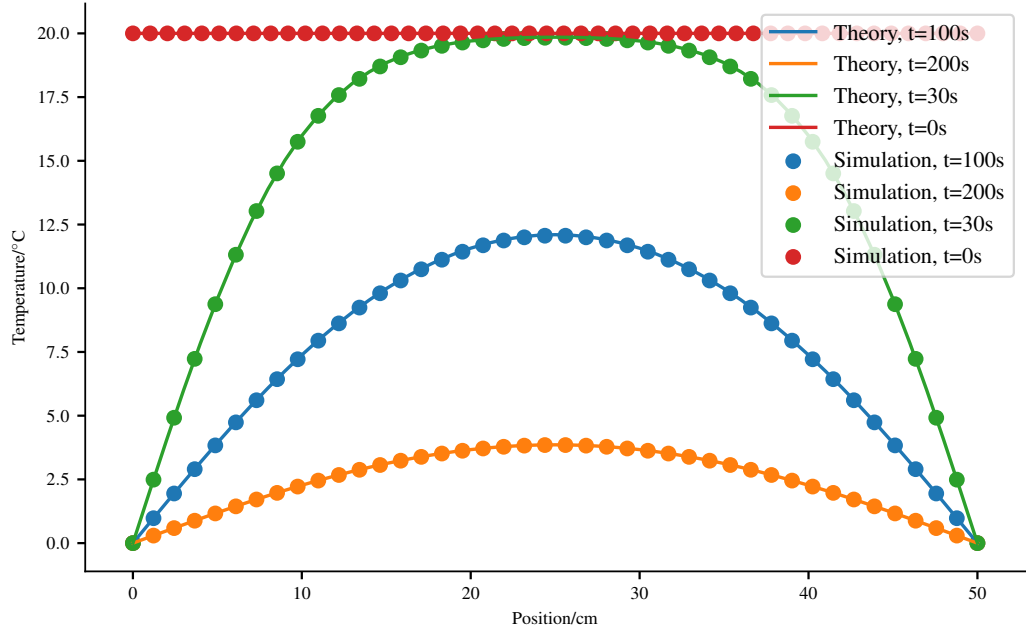


**Figure 1.8:** Temperature of the cube for various times, comparing between analytical solution and numerical method.

Applying the boundary conditions (Eqs. (1.26) and (1.27)) gives:

$$A_1 = B_1 = C_1 = 0 \text{ and } \alpha = \frac{\pi n}{L} \quad \beta = \frac{\pi m}{L} \quad \gamma = \frac{\pi p}{L} \quad (1.30)$$

$$\therefore T_{nmp}(x, y, z, t) = A_{nmp} \cdot \sin\left(\frac{\pi nx}{L}\right) \cdot \sin\left(\frac{\pi my}{L}\right) \cdot \sin\left(\frac{\pi pz}{L}\right) \quad (1.31)$$

This yields the following solution for the heat equation using the principle of superposition, and solving Eq. (1.32) with  $f(x, y, z)$  as the initial temperature profile of the cube:

$$A_{nmp} = \frac{8}{L^3} \int_0^L \int_0^L \int_0^L f(x, y, z) \cdot \sin\left(\frac{\pi nx}{L}\right) \cdot \sin\left(\frac{\pi my}{L}\right) \cdot \sin\left(\frac{\pi pz}{L}\right) dx \cdot dy \cdot dz \quad (1.32)$$

$$T(x, y, z, t) = \sum_{n=1,3,\dots}^{\infty} \sum_{m=1,3,\dots}^{\infty} \sum_{p=1,3,\dots}^{\infty} \frac{2368}{\pi^3 nmp} \cdot \sin\left(\frac{\pi nx}{L}\right) \cdot \sin\left(\frac{\pi my}{L}\right) \cdot \sin\left(\frac{\pi pz}{L}\right) \cdot e^{(-\lambda^2 t)} \quad (1.33)$$

Where:

$\lambda^2 = \alpha\pi^2\left(\frac{n^2}{L^2} + \frac{m^2}{L^2} + \frac{p^2}{L^2}\right);$   
 $n, m, p$  are odd integers;  
and  $L$  is the length of the cube.

A slice through the middle of the cube,  $L = 50 \text{ cm}$ , yields Fig. 1.8, which shows that the numerical method matches the analytical solution closely.

## MCRT and heat transport validation

As a first test of the code, both MCRT and heat simulation, is compared to a simple analytical model of ablation. The simple model of ablation is as: the ablation energy ( $E_a$ ), is defined as the minimum energy required to raise the temperature of the medium to 100 °C, and then boil off the water in a volume  $dV$ , mass  $M$ . Thus, in one dimension Eq. (1.34), where the symbols have their usual meanings. If the energy for ablation is delivered in a time  $dt$  by a laser of intensity ( $Wcm^{-2}$ ),  $P$ , this gives Eq. (1.35). Equation (1.35) can be rearranged to give an ablation front velocity, Eq. (1.36).

$$E_a = c_p \rho dx \Delta T + L_v \rho dx \quad (1.34)$$

$$P \cdot dt = \rho dx (c_p \Delta T + L_v) \quad (1.35)$$

$$u = \frac{P}{\rho(c_p \Delta T + L_v)} \quad (1.36)$$

Assuming the ablation front moves with constant velocity during the ablation, and using  $L_v = 2.53 \cdot 10^6 Jkg^{-1}$ ,  $c_p = 4181 J \cdot kg^{-1} \cdot K^{-1}$  and the medium is a cube side 2 mm, with a starting temperature is 37 °C with a water content of 70% giving a density of  $700 kg \cdot m^{-3}$ . For these parameters this gives an ablation velocity,  $u \simeq 0.77 cm \cdot s^{-1}$ , and a time to ablate through 2 mm of tissue of  $\simeq 0.26 s$ . As the code developed in this chapter simulates the diffusion of heat in a medium due to an incident laser, the expected time to ablate through the same medium should be slightly larger as heat diffuses away from the voxel while it is being heated. When the full heat + MCRT code is used to simulate this experiment, it gives a time,  $t \simeq 0.33 s$ .

## 1.3 *In silico* results

### 1.3.1 Introduction

To match the experimental results, an accurate model of the experimental setup *in silico* must be created. However, due to computational constraints, such as memory and time available, some approximations to the experimental set-up have to be made. The porcine skin was a large thin slice of the top most layers of the skin. However, as the area of interest is where the ablation occurs, initially the porcine skin is modelled as a cuboid, dimensions:  $1.1 \times 1.1 \times 0.5 cm$ . The initial temperature of the porcine skin is assumed to be around 5°, as the tissue was kept on ice or was kept cooled. As mentioned in the previous sections, there are several unknowns in the model:  $T_a$ , water content, temperature of air after ablation, and the exact thermal and optical properties of the porcine tissue. Therefore several models are run so that the full parameter space of these unknowns can be explored. Results from these *in silico* experiments are presented in this section along with a comparison of the model to the experimental work carried out in collaboration with the University of Dundee and the Photobiology department at Ninewells Hospital.

### Optical & thermal properties

The thermal and optical properties of porcine tissue are not known exactly for any given tissue sample. As such the thermal and optical properties used in this section are taken from various literature sources.

The laser used in the experimental work is an CO<sub>2</sub> laser operating at 10.6  $\mu m$ . This means that the optical properties of the tissue are dominated by water absorption. The laser used in the experiment is the Pixel CO<sub>2</sub> [40]. The Pixel CO<sub>2</sub> laser has a wavelength 10.6  $\mu m$  which

	Thermal conductivity, $\kappa$	Density, $\rho$	Heat capacity, $c$
Tissue	$\rho \cdot (6.28 \cdot 10^{-4} \cdot W + 1.17 \cdot 10^{-4} \cdot P)$	$\frac{1000}{W+0.649 \cdot P}$	$4.2 \cdot 10^3 \cdot W + 1.09 \cdot 10^3 \cdot P$
Air	$ae^{-b(T-273.15)} + c$	$\frac{p_{atm}}{R_{spec}T}$	1006

**Table 1.1:** Optical and thermal properties for porcine tissue and air.  $W$  and  $P$  are the percentage of water and protein respectively.  $\rho$  is the density of the skin,  $p_{atm}$  is the pressure of air at 1 atmosphere, and  $R_{spec}$  is the gas constant.  $a$ ,  $b$ , and  $c$  are constants.

corresponds to an absorption of coefficient in water of  $\sim 850 \text{ cm}^{-1}$ . As the absorption coefficient is large, it is assumed that scattering is negligible at these wavelengths. Table 1.1 summarises the thermal properties for tissue and air used in the simulations.

The laser was used in “Pixel beam” mode. This means that the laser beam is split into an array of smaller beams. The laser used an array  $9 \times 9$  of 81 pixel beams, each with a diameter of  $250 \text{ }\mu\text{m}$ . The Pixel  $\text{CO}_2$  rated laser power is  $\sim 70 \text{ W}$ .

The laser delivered one single pulse of varying total energy delivered over the range  $50 \text{ mJ}$  to  $400 \text{ mJ}$ , in so called “super pulsed mode”. The experiment consisted of ablating the porcine tissue, as a function of energy per “pixel” beam. This was achieved by adjusting the pulse length of the laser,  $\tau$ , so that the energy per pulse was varied over a range  $50 \text{ mJ}$  to  $400 \text{ mJ}$ .

### Computational speed up:

As discussed in the Section 1.1, the volume of interest is the area around the ablation craters. The volume is  $1.1 \text{ cm} \times 1.1 \text{ cm} \times 0.5 \text{ cm}$ . However, for the simulation to have good resolution of the ablation craters this volume would require many voxels for the tissue model. This is unfeasible due to: the memory required to store the various counters, grids, and variables, and the time that would be required to carry out the computation. Thus, the volume of interest is reduced to focus on just one of the ablation craters that is created by the laser (a volume of  $0.06 \text{ cm} \times 0.06 \text{ cm} \times 0.18 \text{ cm}$ ) As a check to ensure that no physical phenomena are omitted by focusing on just one ablation crater, an initial simulation that models the full volume of interest was carried out to investigate the possibility of overlapping craters or other related phenomena. The simulation, as shown in Fig. 1.9, gives reassurance that the shrinking of the volume of interest is a valid approximation to make as there is no overlap between the separate ablation crater.

## 1.3.2 Results

### Investigating ablation temperature, $T_a$

Various literature sources report the ablation temperature ranging widely from  $177^\circ$  to  $500^\circ$  [27, 29, 30]. Thus, several models are run over this range to establish the  $T_a$  which fits the experimental results. Figures 1.10 and 1.11 show how  $T_a$ , and beam profile affect the crater depth as a function of pixel beam energy for the  $\text{CO}_2$  laser. The data suggests that, a  $T_a$  around  $T_a = 500^\circ \text{C}$  is appropriate for the studies carried out, the upper limit of  $T_a$  from the literature.

Increasing the ablation temperature has the obvious effect of requiring more energy to be deposited by the laser before ablation takes place. This also allows more heat to diffuse away from the ablation crater increasing the thermal damage done to the surrounding tissue. Decreasing the ablation temperature has the converse affect, and allows the ablation crater to become deeper.

Over the full range of  $T_a$ , as the energy per pixel beam increases, there is a trend that at higher energies the crater depth begins to taper off. This is potentially due to several reasons. As the ablation craters grows the volume of tissue that is ablated is replaced with air, allowing

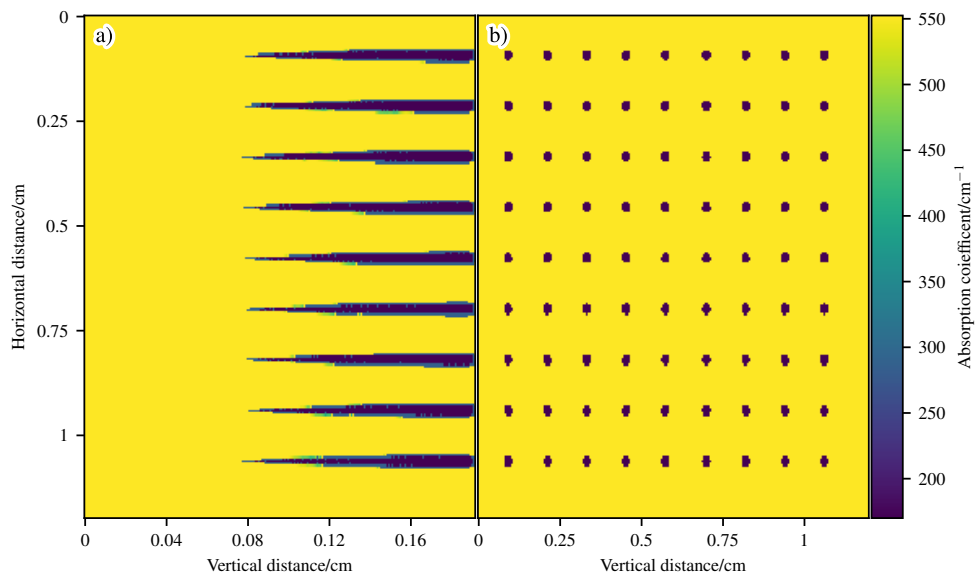


**Figure 1.9:** Simulation of 81 pixel beams. Figure a) shows a slice through the optical properties at the end of the simulation in the z-y plane. Figure b) shows the optical properties in the x-y plane at the top surface. Yellow is unchanged tissue, and purple is completely ablated tissue. Figure shows that the ablation craters do not overlap one another.

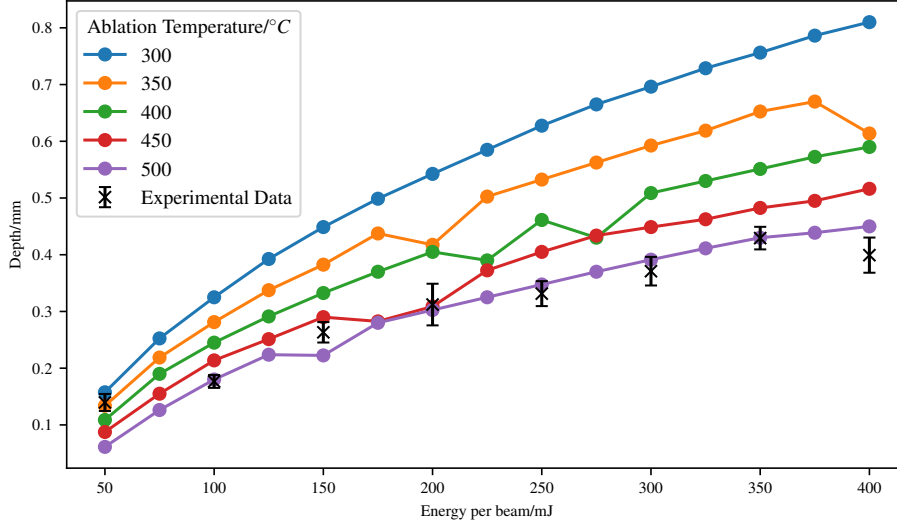


**Figure 1.10:** Simulation of 70 W  $\text{CO}_2$  ablative laser, with a circular beam profile. Crater depths as a function of pixel beam energy for various  $T_a$ ’s.

more heat loss from the tissue to the environment. As well as heat loss to the environment, more heat is diffused away into the surrounding tissue as the crater grow, due to the availability of more tissue for the heat to diffuse into.

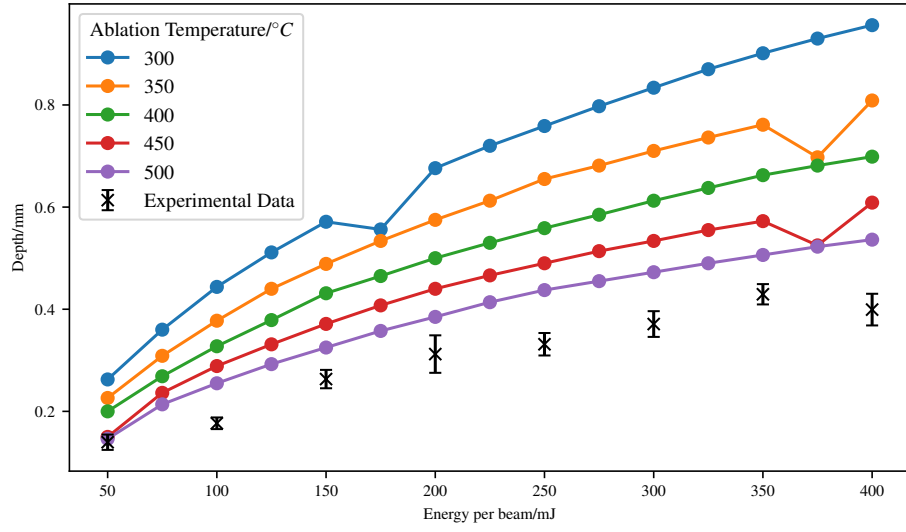
### Temperature during ablation

Figure 1.12 shows slices of temperature as a function of time during a simulation for  $T_a = 500$  °C. This means that every column of pixels shows a bore hole through the medium (along the z axis) for a given time. Figure 1.12 also shows the laser pulse profile as a function of time as a reference so that knowledge of when the laser is on or off is easily elucidated. The figure shows that the temperature reaches a maximum temperature which is equal to  $T_a$ , regardless of ablation progress. This maximum temperature is researched roughly 0.25 s into the simulation, and lasts until  $\sim 0.75$  s. The maximum temperature The ablation crater depth can be seen by the evidence of the “dark valley” before the jump in temperature. The border of the crater region is slightly cooler, with a maximum slightly deeper into the tissue. This temperature maximum extends for a small distance into the tissue, before diffusion spreads it out.

Once the laser reaches maximum power

### Investigating thermal damage

As stated in Section 1.2.3, the Arrhenius damage integral is used to estimate the thermal damage due to the laser. To calculate the tissue damage around the ablation craters, Eq. (1.18) is first transformed into a summation:



**Figure 1.11:** Simulation of 70 W CO<sub>2</sub> ablative laser, with a Gaussian beam profile. Crater depths as a function of pixel beam energy for various  $T_a$  's.

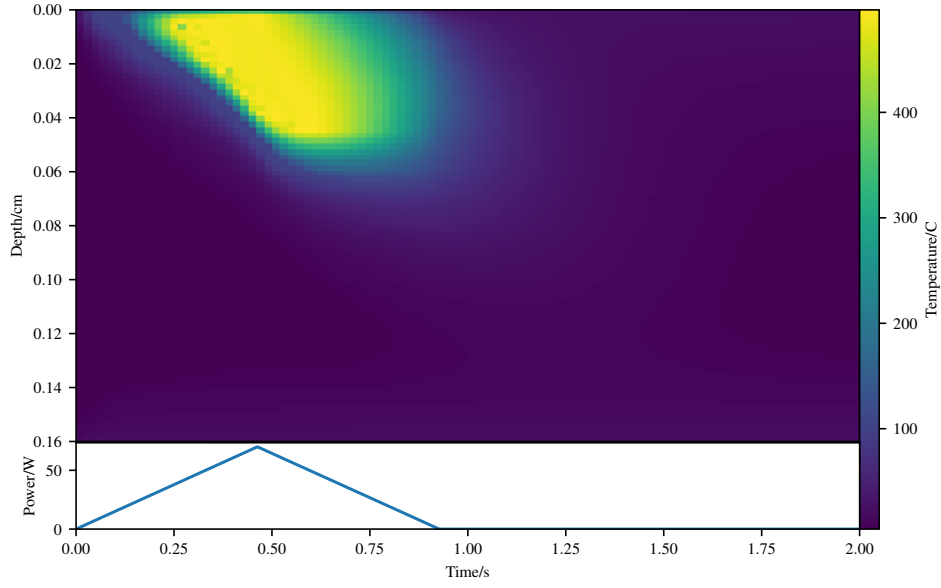


**Figure 1.12:** Temperature bore hole through centre of medium as a function of time, for  $T_a=500$  °C.

$$\Omega(t) = \int_{t_p}^{t_f} Ae^{(-\frac{\Delta E}{RT})} d\tau \quad (1.37)$$

$$\Omega(t) = \sum_{m=m_p}^{m_f} Ae^{(-\frac{\Delta E}{RT_{\xi}^m})} \Delta t \quad (1.38)$$

Where:

$\Delta E$ ,  $R$ ,  $T$ , and  $A$  have the same meanings as before;

$\xi$  is the  $i^{th}, j^{th}, k^{th}$  node;

and  $m_p$  is the  $p^{th}$  timestep when the  $\xi^{th}$  node is above the threshold temperature.

Using Eq. (1.38) it can thus be estimated that the damage to the tissue on a voxel by voxel basis. Figure 1.13 shows how far the thermal damage extends around the ablation crater. For ease of visualisation 1-3 is mapped to their respective burns via the following scheme, with  $\eta$  as burn severity:

$$\eta = \begin{cases} 3, & \Omega \geq 10000 \\ 2, & 1 \leq \Omega < 10000 \\ 1, & 0.53 \leq \Omega < 1 \\ 0, & 0.0 \leq \Omega < 0.53. \end{cases} \quad (1.39)$$

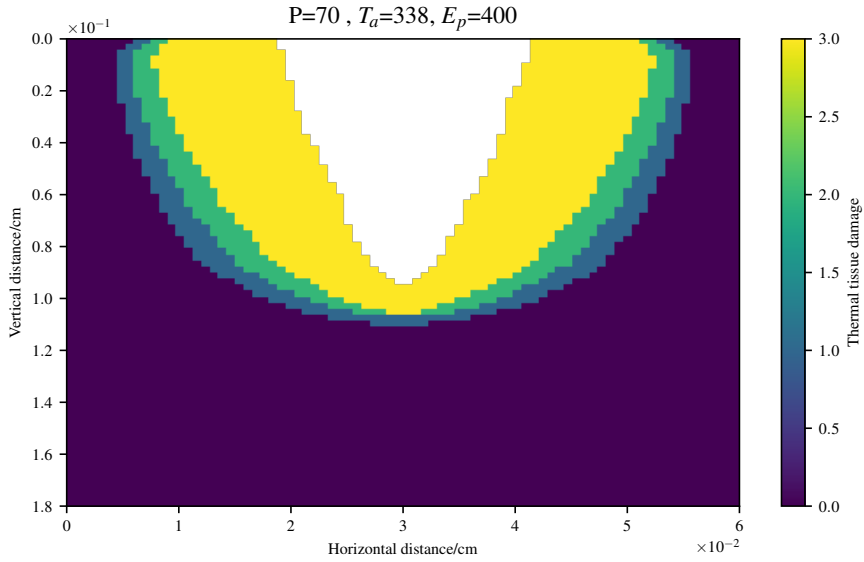


**Figure 1.13:** Tissue thermal damage around the ablation crater (white). Thermal tissue damage values of 3 refer to 3<sup>rd</sup> degree burns, 2 to 2<sup>nd</sup>, and 1 to 1<sup>st</sup> degree burns respectively.  $P$  is the power in Watts,  $T_a$  is the ablation temperature in Kelvin, and  $E_p$  is the energy per pixel beam in mJ.

As shown in Fig. 1.13, the thermal damage zone extends for a small distance around the ablation crater, due to the diffusion of heat into these areas. Figure 1.14 shows the maximum horizontal thermal damage distance as a function of  $T_a$ , and pixel beam energy. For values of  $T_a$  less than  $\sim 425$  °C, it appears that the maximum horizontal extent of the thermal damage tapers off. This is most likely because for lower values of  $T_a$ , there is a larger ablation crater, meaning that the energy from the laser is deposited deeper in the tissue in comparison to higher values of  $T_a$ . The higher values of  $T_a$  allow greater diffusion of the heat, thus yielding larger zones of damage. Overall there is little difference in the maximum horizontal extent of thermal injury, when using different energies (of the order of  $\sim 0.01$  mm).



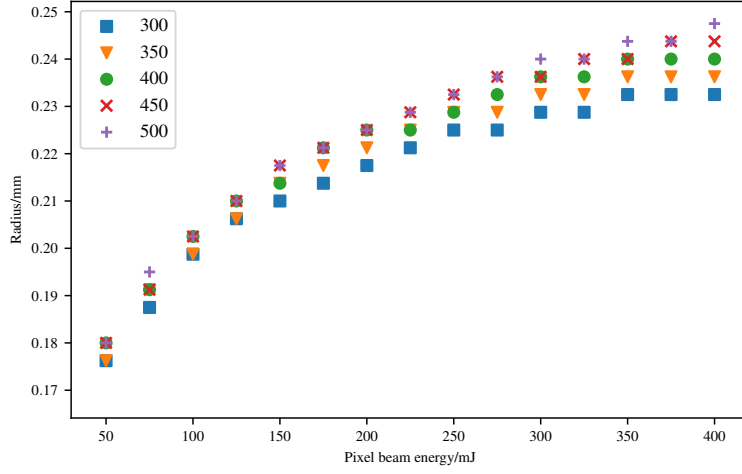


**Figure 1.14:** Figure shows the maximum horizontal extent of thermal damage as a function of energy per pixel beam, for different  $T_a$  's.

Investigations for the time it takes for different areas of the tissue to become thermally damaged, were also carried out. This can be easily achieved by saving the time each voxel passes one of the damage boundaries in Eq. (1.39). Figures 1.15 and 1.16 show the minimum time taken for 1<sup>st</sup>, 2<sup>nd</sup>, and 3<sup>rd</sup> degree burns to occur as a function of depth. Figure 1.15 shows that there is little to no time (upon the order of 0.5 ms) between 1<sup>st</sup> and 2<sup>nd</sup>, and 3<sup>rd</sup> degree burns. Figure 1.16 shows there is a slightly greater time difference between 1<sup>st</sup> and 2<sup>nd</sup>, and 3<sup>rd</sup> degree burns, however this is almost as negligible as the 400 mJ case.

The reason that there is almost no time between 1<sup>st</sup> and 2<sup>nd</sup>, and 3<sup>rd</sup> degree burns, is most likely because there is little time for heat to diffuse, whilst the laser is still illuminating the medium. The laser pulses are on the order of seconds, and tissue is not thermally conductive. This leads to the results presented here.

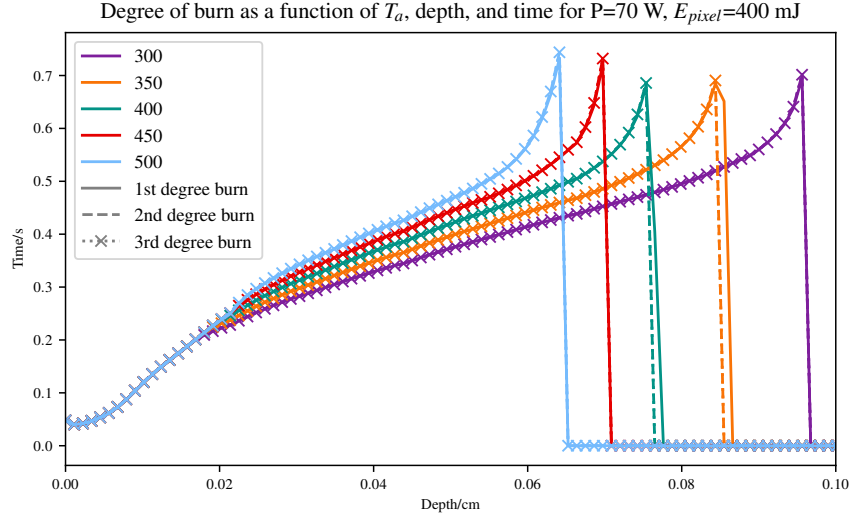


**Figure 1.15:** Figure show the time taken for 1<sup>st</sup>, 2<sup>nd</sup>, and 3<sup>rd</sup> to occur as a function of depth, for a range of  $T_a$ 's at 400 mJ.

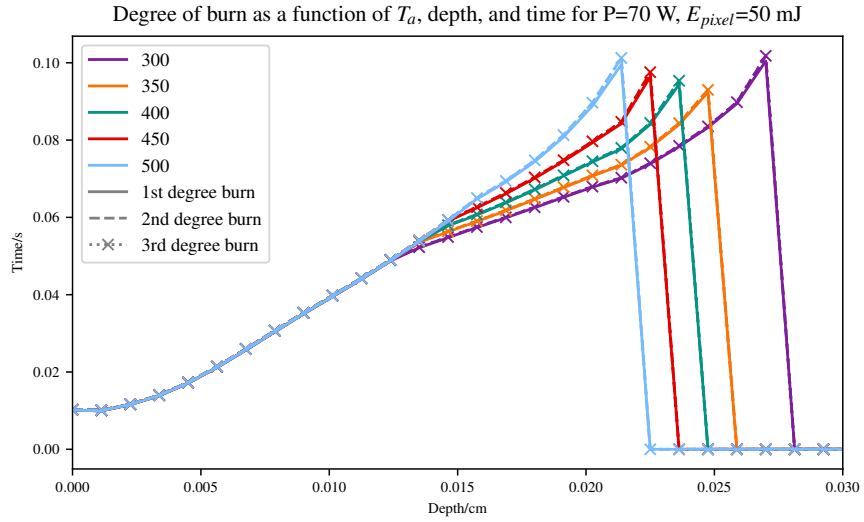


**Figure 1.16:** Figure show the time taken for 1<sup>st</sup>, 2<sup>nd</sup>, and 3<sup>rd</sup> to occur as a function of depth, for a range of  $T_a$ 's at 50 mJ.

### Investigating beam type

As the manufacturer does not provide information on the beam profile of the pixel beams and the lack of equipment available to measure the beam profile, the shape of the beam profile has to be assumed. Two different beam types are tried: Gaussian and circular (top-hat). Figures 1.10 and 1.11 show the result of these *in-silico* experiments. The Gaussian beam ablates deeper holes than the circular beam type, which is to be expected due to the distribution of power in the

Gaussian beam. The beam that best fits the data is the circular beam. For the Gaussian beam to fit the data ablation would have to take place at temperatures above  $500\text{ }^{\circ}\text{C}$  which does not fit with the literature. Without knowing the exact profile of the beam, it is assumed for the rest of the *in-silico* experiments that the beam profile is circular.

### Investigating laser pulse profile

Pulsed lasers have a variety of pulse profiles. The pulse profiles are usually modelled as triangular, tophat, or Gaussian. However, the pulse profiles in reality are normally less well defined, and rather the pulse profile is something in between these perfect models.

The laser used in the above experiments, the Pixel  $\text{CO}_2$ , uses a triangular pulse profile for the laser pulses. Thus, in this section the effect of the laser pulse profile has on ablation and the surrounding thermal injury is investigated.

Four different laser pulses profiles are investigated: tophat, triangular and two different Gaussian profiles. The two different Gaussian pulses trialled are, a Gaussian profile with  $\sigma$  equal to the pulselength, and a pulse profile where the same energy is expended.

Figure 1.17 show the pulse profiles for a pulselength of  $0.2\text{ s}$ .

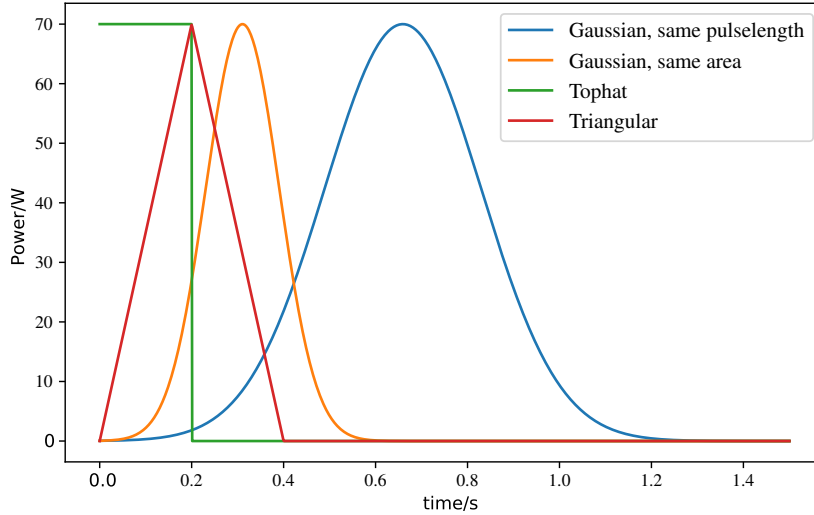


**Figure 1.17:** Comparison of the different pulse profiles trialled for a pulselength of  $0.2\text{ s}$ .

#### 1.3.2.1 Investigating Initial Temperature

As the experiment was carried out on porcine tissue that was kept on ice before the experiment was conducted, we assumed that the initial temperature of the porcine tissue was around  $5\text{ }^{\circ}\text{C}$ . This section investigates whether this is an accurate assumption.

To investigate this, three different temperatures were trialled:  $0\text{ }^{\circ}\text{C}$ ,  $5\text{ }^{\circ}\text{C}$ , and  $25\text{ }^{\circ}\text{C}$ . These temperature correspond to room temperature, the temperature of ice and the original temperature we assumed. Figure 1.19 shows the results of this *in-silico* investigation.

As expected the hotter the porcine skin is initially the larger the ablation depth. This occurs as less energy is required to bring the porcine skin to its ablation temperature. In the previous subsections it was assumed that the temperature of the porcine skin was around  $5\text{ }^{\circ}\text{C}$ . This assumption was based upon the fact that the porcine skin was kept on ice before the experiment,

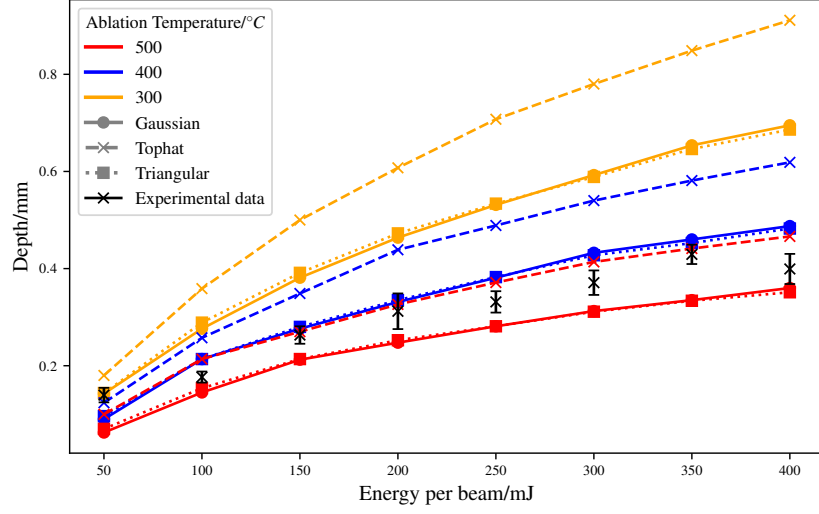


**Figure 1.18:** Comparison of various pulse shapes for the pixel beams.

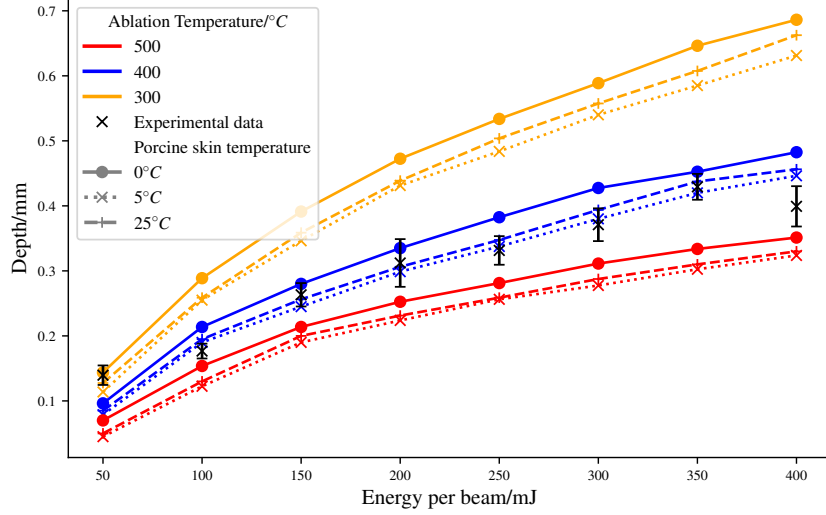


**Figure 1.19:** Comparison of ablation depths for different initial temperatures in the porcine skin.

thus the temperature of the skin must be between 0 and room temperature. This investigation shows that over small variations of temperature ( $\lesssim 5^\circ\text{C}$ ), the ablation depth does not vary too much (on the order of  $\approx 0.01\text{ mm}$ ).

However, there is a greater difference in the maximum extent of thermal damage to the skin for different initial temperatures in the porcine skin. Figure 1.20 shows this difference.

### 1.3.2.2 Investigating Voxel Temperature After Ablation

In the previous section it is assumed that the temperature of a voxel remains unchanged after the tissue is removed from that voxel via ablation. However, this assumption may not be accurate.

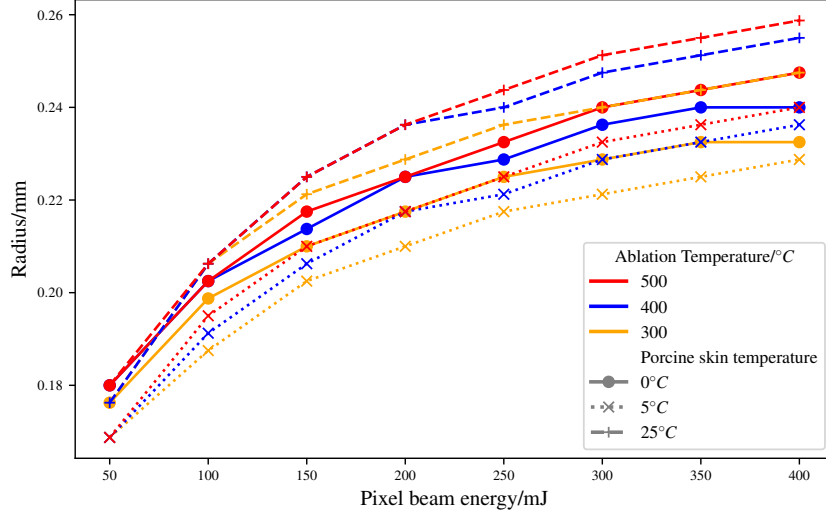


**Figure 1.20:** Comparison of maximum horizontal damage distance for different initial porcine skin temperatures.

To test if the temperature of the voxel after ablation effects the depth of ablation or the thermal injury to the surrounding tissue various voxel temperature were tried. Two different temperatures were tried: half the ablation temperature and room temperature ( $\approx 25^\circ\text{C}$ ). Figure 1.21 shows the effect of the voxel temperature after ablation has on the ablation depth.

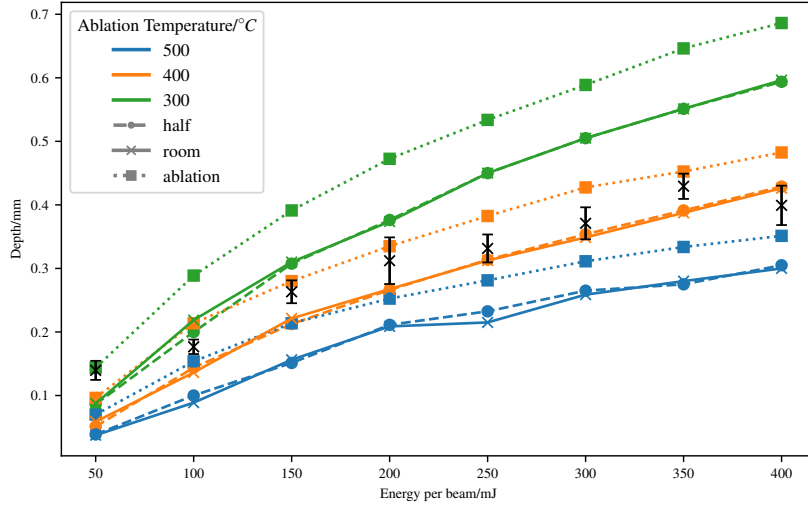


**Figure 1.21:** Comparison of different voxel temperatures after ablation. Half refers to setting the temperature of a voxel to half that of the ablation temperature. Room refers to room temperature, and ablation leaves the temperature at the ablation temperature.

Setting the voxel temperature to either half the ablation temperature or to room temperature has a large effect on the ablation depth, with a difference of  $\approx 0.1\text{ mm}$ . However, there is a small difference between setting the voxel temperature to room temperature and to half of the

ablation temperature though.

## 1.4 Application of Model for Spy Disposal

In the 1964 James Bond film, Goldfinger, James Bond is threatened with a laser by the titular antagonist (Fig. 1.22). Would this laser actually cut Bond in half as the film implies, and could Goldfinger be more humane<sup>†</sup> in his choice of laser for the task?

As the first laser was demonstrated in 1960 was a ruby laser of 694 nm, with the film being released in 1964 and the “laser”<sup>‡</sup> shown on screen being red, the likely laser portrayed is a ruby laser.

To assess whether Bond would die due to the laser we used the model outlined in this chapter with the following parameters.

As Auric Goldfinger uses this laser to cut sheets of gold, we assumed the power of the laser was around 1 kW, as industrial lasers used to cut metal, are high powered continuous operation lasers. We assumed that the Bond is completely made of skin, with no organs or bones. We ran two simulations, one for the Ruby 694 nm and one for the CO<sub>2</sub> 10.6 μm. For the CO<sub>2</sub> as before there is no scattering due to high absorption coefficient. The Ruby laser’s wavelength is highly scattering, so we model both scattering and absorption. The medium we model is a 2 cm<sup>3</sup> cube of homogeneous skin.

We found that the CO<sub>2</sub> takes 22 ms, and Ruby takes 11 s to ablate through the 2 cm medium. From timing the movie, the laser moves at a round 1 cm s<sup>-1</sup>. Therefore the Ruby laser used by Goldfinger would only give Bond some serious burns, but would leave him in one piece. If Goldfinger used a CO<sub>2</sub> laser then Bond would have been cleanly cut in two.

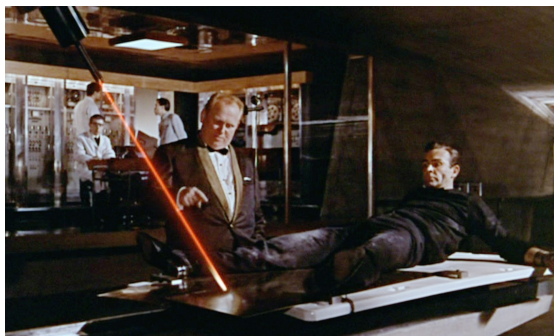


**Figure 1.22:** Still image of the iconic laser scene in the film Goldfinger. Copyrights Eon Productions.

## 1.5 Conclusion

Using MCRT and a finite difference method, a fully 3D model of photon and heat transport within tissue has been created. This model can be used to simulate the heat deposited by laser, the ablation craters formed via high powered lasers and the resultant thermal damage surrounding the ablation crater.

---

<sup>†</sup>i.e could Goldfinger use a laser that would lessen Bond’s suffering.

<sup>‡</sup>A laser was not used on set, but rather was added in post-production.

The model has been fully compared with both analytical solutions and experimental results. The model was found to match with experimental results that a tissue ablation temperature  $T_a$  of around  $500\text{ }^{\circ}\text{C}$  has to be adopted, towards the higher end of the range previously observed in the literature.

The simulations allow us to predict for a given laser power and pulse length, how much thermal damage is caused in the tissue, and how deep an ablation crater that will form. The computational model could be used in future to help develop treatment regimes for both aesthetic and medical procedures. For example, currently there is considerable amount of “down time” after skin rejuvenation, in which the patient displays inflammation, erythema, edema, pain, and crusting [41–43]. Simulations of thermal damage due to fractional ablation could help design treatment regimes that minimise these effects, whilst still delivering skin rejuvenation. The model can also be applied to help optimise laser assisted drug delivery. Laser assisted drug delivery consists of using a laser to “drill” holes into the skin to help topical medicines diffuse into the skin better, than just applying the medicines to skin with no holes. Our model can help predict the laser parameters needed to reach a certain hole depth, thus minimising thermal damage and pain to patients.

There are many avenues available with regards to future work on this model. The model presented here in this chapter was on a initially homogeneous skin model. In reality skin is compromised of several distinctive layers, with each layer containing varying amounts of different chromophores. Our model can easily incorporate an multi-layered skin model complete with various fractions of chromophores. However, as the laser used in these studies is an infra-red laser, water is the highest absorbing chromophore, meaning that a physically accurate model, with various chromophores is not need for this application. The current model is a voxel based model, where all the voxels are the same size. This allows the model presented in this chapter to be easily set-up, with regards to parallelisation, optical/thermal properties and ease of programming. However, voxel models, where all the voxels are the same size, are not computationally efficient. Particularly in order to achieve good resolution, many voxels are needed, which requires large amounts of RAM, due to a  $\sim n^3$  scaling of voxels to memory in 3D. A more efficient way, would be to allow different sizes of voxels, depending on parts of the model which need high resolution, and parts that do not need high resolution. Such a voxel model is called an adaptive mesh refinement (AMR). There are downsides to AMR: complex implementation for parallelisation and set-up of optical/thermal properties, slower optical depth integration routines due to neighbour lookups.





# Bibliography

- [1] D. Manstein, G.S. Herron, R.K. Sink, H. Tanner, and R.R. Anderson. Fractional photothermolysis: a new concept for cutaneous remodeling using microscopic patterns of thermal injury. *Lasers in Surgery and Medicine: The Official Journal of the American Society for Laser Medicine and Surgery*, 34(5):426–438, 2004.
- [2] S. Amini-Nik, D. Kraemer, M.L. Cowan, K. Gunaratne, P. Nadesan, B.A. Alman, and R.J. Dwayne Miller. Ultrafast mid-ir laser scalpel: protein signals of the fundamental limits to minimally invasive surgery. *PLoS One*, 5(9):e13053, 2010.
- [3] O.T. Tan, K. Sherwood, and B.A. Gilchrest. Treatment of children with port-wine stains using the flashlamp-pulsed tunable dye laser. *New England Journal of Medicine*, 320(7):416–421, 1989.
- [4] M. Kuperman-Beadle, V.J. Levine, and R. Ashinoff. Laser removal of tattoos. *American Journal of Clinical Dermatology*, 2(1):21–25, 2001.
- [5] S.H. Liew. Laser hair removal. *American Journal of Clinical Dermatology*, 3(2):107–115, 2002.
- [6] C.A. Hardaway and E.V. Ross. Nonablative laser skin remodeling. *Dermatologic Clinics*, 20(1):97–111, 2002.
- [7] S.M. Shapshay, M.S. Strong, G.W. Anastasi, and C.W. Vaughan. Removal of rhinophyma with the carbon dioxide laser: a preliminary report. *Archives of Otolaryngology*, 106(5):257–259, 1980.
- [8] R. Valcavi, F. Riganti, A. Bertani, D. Formisano, and C.M. Pacella. Percutaneous laser ablation of cold benign thyroid nodules: a 3-year follow-up study in 122 patients. *Thyroid*, 20(11):1253–1261, 2010.
- [9] M. Hædersdal, F.H. Sakamoto, W.A. Farinelli, A.G. Doukas, J. Tam, and R.R. Anderson. Fractional CO<sub>2</sub> laser-assisted drug delivery. *Lasers in Surgery and Medicine: The Official Journal of the American Society for Laser Medicine and Surgery*, 42(2):113–122, 2010.
- [10] M.R. Alexiades-Armenakas, J.S. Dover, and K.A. Arndt. The spectrum of laser skin resurfacing: nonablative, fractional, and ablative laser resurfacing. *Journal of the American Academy of Dermatology*, 58(5):719–737, 2008.
- [11] D.V. Widder. *The Heat Equation*, volume 67. Academic Press, 1976.
- [12] N. Ozisik. *Finite Difference Methods in Heat Transfer*. CRC press, 1994.

- [13] Alma Lasers GmbH. *PixelCO2 Operator's Manual*. Alma Lasers GmbH.
- [14] Sasko Ristov, Radu Prodan, Marjan Gusev, and Karolj Skala. Superlinear speedup in hpc systems: Why and when? In *Computer Science and Information Systems (FedCSIS), 2016 Federated Conference on*, pages 889–898. IEEE, 2016.
- [15] A.J Welch, M.J.C Van Gemert, et al. *Optical-thermal Response of Laser-irradiated Tissue*, volume 2. Springer, 2011.
- [16] N.T. Wright. Quantitative models of thermal damage to cells and tissues. In *Heat Transfer and Fluid Flow in Biological Processes*, pages 59–76. Elsevier, 2015.
- [17] M.H. Niemz. *Laser-tissue interactions: fundamentals and applications*. Springer Science & Business Media, 2013.
- [18] F. Petrella, S. Cavaliere, and L. Spaggiari. Popcorn effect. *Journal of Bronchology & Interventional Pulmonology*, 20(2):193–194, 2013.
- [19] R.M. Verdaasdonk, C. Borst, and M.J.C. Van Gemert. Explosive onset of continuous wave laser tissue ablation. *Physics in Medicine & Biology*, 35(8):1129, 1990.
- [20] W Husinsky, G Grabner, I Baumgartner, F Skorpik, S Mitterer, and T Temmel. Mechanisms of laser ablation of biological tissue. In *Desorption Induced by Electronic Transitions DIET IV*, pages 362–367. Springer, 1990.
- [21] Moishe S Kitai, Valery L Popkov, VA Semchischen, and Alexei A Kharizov. The physics of uv laser cornea ablation. *IEEE journal of quantum electronics*, 27(2):302–307, 1991.
- [22] Alexander A Oraevsky, Rinat O Esenaliev, and Vladilen S Letokhov. Pulsed laser ablation of biological tissue: Review of the mechanisms. In *Laser Ablation Mechanisms and Applications*, pages 112–122. Springer, 1991.
- [23] A. Vogel and V. Venugopalan. Mechanisms of pulsed laser ablation of biological tissues. *Chemical Reviews*, 103(2):577–644, 2003.
- [24] G Koren and JTC Yeh. Emission spectra, surface quality, and mechanism of excimer laser etching of polyimide films. *Applied Physics Letters*, 44(12):1112–1114, 1984.
- [25] JE Andrew, PE Dyer, D Forster, and PH Key. Direct etching of polymeric materials using a xecl laser. *Applied Physics Letters*, 43(8):717–719, 1983.
- [26] A.L. McKenzie. Physics of thermal processes in laser-tissue interaction. *Physics in Medicine & Biology*, 35(9):1175, 1990.
- [27] A.L. McKenzie. A three-zone model of soft-tissue damage by a CO2 laser. *Physics in Medicine & Biology*, 31(9):967, 1986.
- [28] Boris Majaron, P Plestenjak, and Matjaž Lukač. Thermo-mechanical laser ablation of soft biological tissue: modeling the micro-explosions. *Applied Physics B*, 69(1):71–80, 1999.
- [29] M. Gerstmann, Y. Linenberg, A. Katzir, and S. Akselrod. Char formation in tissue irradiated with a CO 2 laser: model and simulations. *Optical Engineering*, 33(7):2343–2352, 1994.
- [30] A. Sagi, A. Avidor-Zehavi, A. Shitzer, M. Gerstmann, S. Akselrod, and A. Katzir. Heating of biological tissue by laser irradiation: temperature distribution during laser ablation. *Opt. Eng.*, 31(7):1425–1431, 1992.

- [31] J.A. Pearce. Relationship between arrhenius models of thermal damage and the cem 43 thermal dose. In *Energy-based Treatment of Tissue and Assessment V*, volume 7181, page 718104. International Society for Optics and Photonics, 2009.
- [32] F.C. Jr Hendriques. Studies of thermal injury; the predictability and the significance of thermally induced rate processes leading to irreversible epidermal injury. *Arch. Pathol.(Chic)*, 43:489–502, 1947.
- [33] S.C. Jiang, N. Ma, H.J. Li, and X.X. Zhang. Effects of thermal properties and geometrical dimensions on skin burn injuries. *Burns*, 28(8):713–717, 2002.
- [34] K.R. Diller and L.J. Hayes. A finite element model of burn injury in blood-perfused skin. *Journal of Biomechanical Engineering*, 105(3):300–307, 1983.
- [35] Ji-zhuang Zhang and Xue-xue Zhang. Dynamic modeling of tissue ablation with continuous wave co2 laser. In *2007 1st International Conference on Bioinformatics and Biomedical Engineering*, pages 1057–1060. IEEE, 2007.
- [36] I.V. Meglinski and S.J. Matcher. Quantitative assessment of skin layers absorption and skin reflectance spectra simulation in the visible and near-infrared spectral regions. *Physiological Measurement*, 23(4):741, 2002.
- [37] B.R. Loiola, H.R.B. Orlande, and G.S. Dulikravich. Thermal damage during ablation of biological tissues. *Numerical Heat Transfer, Part A: Applications*, pages 1–17, 2018.
- [38] Valentina Casalegno, P Vavassori, M Valle, M Ferraris, M Salvo, and G Pintsuk. Measurement of thermal properties of a ceramic/metal joint by laser flash method. *Journal of Nuclear Materials*, 407(2):83–87, 2010.
- [39] E MacCormack, A Mandelis, M Munidasa, B Farahbakhsh, and H Sang. Measurements of the thermal diffusivity of aluminum using frequency-scanned, transient, and rate window photothermal radiometry. theory and experiment. *International journal of thermophysics*, 18(1):221–250, 1997.
- [40] Alma Lasers. Pixel CO2, 2018.
- [41] M. Lapidoth, S. Halachmi, S. Cohen, and D.B. Amitai. Fractional co2 laser in the treatment of facial scars in children. *Lasers in Medical Science*, 29(2):855–857, 2014.
- [42] M.A. Trelles, M. Shohat, and F. Urdiales. Safe and effective one-session fractional skin resurfacing using a carbon dioxide laser device in super-pulse mode: a clinical and histologic study. *Aesthetic Plastic Surgery*, 35(1):31–42, 2011.
- [43] E. Kohl, J. Meierhöfer, M. Koller, F. Zeman, L. Groesser, S. Karrer, U. Hohenleutner, M. Landthaler, and S. Hohenleutner. Fractional carbon dioxide laser resurfacing of rhytides and photoaged skin—a prospective clinical study on patient expectation and satisfaction. *Lasers in Surgery and Medicine*, 47(2):111–119, 2015.